Turbulence suppression and regeneration in a magnetohydrodynamic duct flow due to influence of arbitrary electrically conductive walls

Blishchik, Artem; Kenjereš, Saša

DOI
10.1063/5.0084442

Publication date
2022

Document Version
Final published version

Published in
Physics of Fluids

Physics of Fluids

Turbulence suppression and regeneration in a magnetohydrodynamic duct flow due to influence of arbitrary electrically conductive walls

Cite as: Phys. Fluids **34**, 045101 (2022); https://doi.org/10.1063/5.0084442
Submitted: 06 January 2022 • Accepted: 13 March 2022 • Published Online: 01 April 2022

Artem Blishchik and Saša Kenjereš

Physics of Fluids ARTICLE scitation.org/journal/phf

Turbulence suppression and regeneration in a magnetohydrodynamic duct flow due to influence of arbitrary electrically conductive walls

Cite as: Phys. Fluids **34**, 045101 (2022); doi: 10.1063/5.0084442
Submitted: 6 January 2022 · Accepted: 13 March 2022 ·
Published Online: 1 April 2022

Artem Blishchik and Saša Kenjereš[a)]

AFFILIATIONS

Transport Phenomena Section, Department of Chemical Engineering, Faculty of Applied Sciences, Delft University of Technology and J.M. Burgerscentrum Research School for Fluid Mechanics, Van der Maasweg 9, 2629 HZ Delft, The Netherlands

[a)]Author to whom correspondence should be addressed: S.Kenjeres@tudelft.nl

ABSTRACT

In the current study, we present a series of numerical simulations describing a turbulent magnetohydrodynamic flow subjected to a transverse magnetic field in a square duct with arbitrary electrically conductive walls. The characteristic flow and electromagnetic non-dimensional parameters (Reynolds and Hartmann number, respectively) were fixed, while the wall conductivity ratio (C_d) was varied from the perfectly electrically insulated ($C_d = 0$) to perfectly electrically conducting ($C_d \to \infty$). We have assumed the one-way coupling between the flow of an electrically conducting fluid and the imposed magnetic field. The influence of the electrically conducting walls was imposed by simulating additional finite solid domains coupled with the channel interior. The turbulence was simulated by applying the large eddy simulation approach with the dynamic Smagorinsky sub-grid scale model. The obtained results confirmed a significant impact of the conductivity of the surrounding walls on the flow and turbulence reorganization. We have observed that the initially fully developed turbulence regime was gradually suppressed in the $0 \leq C_d < 0.15$ range, while the fully laminarized state was obtained at $C_d = 0.15$. We found that the process of turbulence suppression was accompanied by the appearance of the patterned turbulence phenomenon in the proximity of the walls parallel to the magnetic field direction. With a further increase in the wall conductivity parameter ($0.15 < C_d < \infty$), we have observed a complete turbulence regeneration. We found that this turbulence regeneration was caused by the local reorganization of the total current density loops near the electrically conducting walls.

I. INTRODUCTION

Starting from the pioneering works of Hartmann and Lazarus[1] and Alfvén,[2] the research field of magnetohydrodynamics (MHD), which addresses interactions between the flow of an electrically conducting fluid and imposed magnetic field, significantly advanced in various fields of the fundamental (plasma) physics and technological applications such as a new generation of fusion reactors,[3–5] continuous casting,[6,7] microfluidic systems,[8–10] etc. Among these applications, MHD turbulence plays an important role. The majority of the MHD turbulence-related studies presented in the literature addressed relatively simple flow geometries including the plane channels, pipes, or ducts.[11] However, the experimental studies of the MHD turbulence are associated with numerous difficulties due to the nontransparent nature of the working fluids characterized by high electrical conductivity (e.g., liquid metals), which requires novel measuring techniques. Additional challenges regarding experimental studies are associated with the potentially high temperatures (continuous casting) and suitable magnetic field generators that are able to provide sufficiently strong magnetic fields. These experimental challenges can be easily removed in numerical studies of the MHD phenomena. However, the numerical studies need to be based on the specific additional prerequirements for the MHD extended Navier–Stokes solver. This includes the conservative form of the pressure and Lorentz force terms in the momentum equation, and the divergence-free conditions of the magnetic induction and total current density, respectively. Furthermore, the proper treatment of the MHD turbulence needs to be performed.[12,13]

To begin with the Reynolds-Averaged Navier–Stokes (RANS) turbulence modeling approach, additional MHD extensions of the two-equation eddy-viscosity based models were proposed.[14] The proposed model was able to correctly describe the turbulence suppression due to imposed magnetic field. The one-equation RANS turbulence

model for quasi-two-dimensional turbulent MHD flow was presented by Smolentsev and Moreau[15] The modified variant of the $k-\omega$ shear stress transport (SSS) turbulence model with additional MHD anisotropy parameter[16] was presented by Miao *et al.*,[17] and applied for simulations of the continuous casting. The full second-moment Reynolds-stress turbulence closure with MHD extensions was presented by Kenjereš *et al.*[18] The model performances were studied in simulating turbulent channel flows subjected to external magnetic fields of different orientations. Good agreement with available direct numerical simulation (DNS) and experimental data was obtained over an extended range of Reynolds and Hartmann numbers.

In recent years, impressive progress was made in applying the high-fidelity eddy-resolving simulations [DNS and large eddy simulation (LES)] of the MHD turbulence. Different sub-grid closures (SGS) were tested in LES simulations of the turbulent MHD channel flow.[19] The dynamic Smagorinsky and originally developed coherent structures based SGS models demonstrated their accuracy and numerical robustness. A combined DNS/LES study was performed by Krasnov *et al.*,[20] where the impact of the uniform spanwise oriented magnetic field on the turbulent MHD channel flow was analyzed. The increased strength of the imposed magnetic field reduced velocity fluctuations and, finally, have produced the full flow laminarization. The DNS study of the turbulent MHD duct was conducted by Chaudhary *et al.*[21] It was observed that the stronger suppression of the turbulence occurred in the proximity of the side walls perpendicular to the imposed magnetic field. Krasnov *et al.*[22] performed the DNS simulations of the turbulent MHD duct flow at very high Reynolds numbers and found a relatively wide range of Hartmann numbers for which the flow was neither fully laminar nor fully turbulent, but with a distinct laminar core. This coexistence of the laminar and turbulent parts of the flow (patterned turbulence) was also addressed in DNS studies of evolving MHD duct and pipe flows by Krasnov *et al.*[23] and Zikanov *et al.*[24] It was demonstrated that using a sufficiently long computational domain was crucial in reproducing the patterned turbulence patterns. The decay of the honeycomb-generated turbulence in a duct due to the influence of the imposed transverse magnetic field was studied by Zikanov *et al.*[25] The paradoxical observation of the high-amplitude velocity fluctuations was explained in terms of the large-scale quasi-two-dimensional flow structures forming, which survived the magnetic suppression. Compressible MHD turbulence was studied by Yang *et al.*[26] The authors investigated which turbulence theories proposed for the incompressible cases would be also valid for compressible cases. An alternative approach to simulate magnetohydrodynamic flows, namely, the one-stage simplified lattice Boltzmann method, was proposed by De Rosis *et al.*[27] The accuracy and computational efficiency of this method were demonstrated, making it a good alternative approach for predicting MHD flows.

Despite this extensive number of the numerical studies in the literature dealing with the turbulent MHD flows, the prevailing majority of the considered cases were with electrically insulated surrounding walls. However, it was recognized that a significant flow reorganization can be generated when the electrically insulated walls were replaced with the walls of a finite electrical conductance.[28] The laminar MHD duct flow with arbitrary electrically conducting walls was numerically simulated by Sterl,[29] and generation of the M-shaped velocity profile was reported. The linear stability analysis of the MHD duct flow was performed by Arlt *et al.*,[30] and a strong dependency between the flow instabilities and imposed Hartmann walls conductance ratio. The MHD duct flows in laminar and turbulent flow regimes at various Hartmann numbers and with a constant value of the wall conductance were presented by Thomas and Bühler[31] The onset of the flow instabilities was investigated and good agreement between simulations and experiments[32] was obtained. In addition to the channel and duct flows, effects of the various wall conductances were also analyzed in different configurations. Effects of the electrically conducting walls on the rotating magnetoconvection were analyzed by Zhang *et al.*[33] When electrically insulated walls were replaced by the walls of finite conductivity, the flow oscillations were suppressed. The MHD mixed convection in micro-channels with one electrically conducting and one electrically insulated wall was analyzed by Akinshilo.[34] It was concluded that an increase in the radiation parameter produced a temperature decrease, with a stronger effect taking place near the electrically conducting wall.

In the present work, we focus on filling the existing gap in the literature dealing with a systematic investigation of effects of the finite electrical conductivity of the side walls in the initially fully developed turbulent flow regime in a square duct. The present contribution is a significantly extended version of our initial findings reported in Blishchik and Kenjereš.[35]

II. GOVERNING EQUATIONS AND NUMERICAL DETAILS

A. One-way coupled MHD flow and turbulence modeling

In the present work, a turbulent flow of an incompressible electrically conductive fluid is considered. The fluid is subjected to an external uniform magnetic field (constant in time), which results in the generation of the active Lorentz force. The conservation laws of the mass and momentum can be formulated as follows:

$$\frac{\partial u_i}{\partial x_i} = 0, \tag{1}$$

$$\frac{\partial u_i}{\partial t} + u_j \frac{\partial u_i}{\partial x_j} = -\frac{1}{\rho}\frac{\partial p}{\partial x_i} + \nu \frac{\partial^2 u_i}{\partial x_j^2} + \frac{1}{\rho} F_i^L, \tag{2}$$

where u_i is velocity, p is pressure, ν is the kinematic viscosity, ρ is density, and $F_i^L = \epsilon_{ijk} J_j B_k$ is the resulting Lorentz force (where J_j is the instantaneous total electric current density and B_k is the imposed magnetic field). Considering the highly turbulent flow, we introduce the large eddy simulation (LES) approach to simulate instantaneous flow and electromagnetic interactions by introducing the following set of the spatially filtered transport equations:

$$\frac{\partial \bar{u}_i}{\partial x_i} = 0, \tag{3}$$

$$\frac{\partial \bar{u}_i}{\partial t} + \bar{u}_j \frac{\partial \bar{u}_i}{\partial x_j} = -\frac{1}{\rho}\frac{\partial \bar{p}}{\partial x_i} + \nu \frac{\partial^2 \bar{u}_i}{\partial x_j^2} - \frac{\partial \tau_{ij}^{sgs}}{\partial x_j} + \frac{1}{\rho} \bar{F}_i^L, \tag{4}$$

where $(\bar{})$ indicates the spatial filtering and τ_{ij}^{sgs} is the sub-grid scale (SGS) stress tensor, which is calculated as

$$\tau_{ij}^{sgs} = -2\nu_{sgs}\bar{S}_{ij}, \quad \nu_{sgs} = (C_S\Delta)^2 (2\bar{S}_{ij}\bar{S}_{ij})^{\frac{1}{2}}, \tag{5}$$

where ν_{sgs} is the sub-grid scale viscosity, S_{ij} is the strain rate tensor, C_S is the Smagorinsky parameter, and Δ is the filter length. The evaluation of C_S becomes crucial since the widely used approach implying

the constant Smagorinsky parameter[36] is not suitable for the present type of flow. It is recognized that the strong influence of the magnetic field affects not only the flow structure but also the turbulence.[37] At the same time, the dynamic determination of C_S is proved to be capable of reproducing this influence.[20] Thus, the dynamic approach originally proposed by Lily[38] has been adopted in our work as follows:

$$C_S^2 = \frac{1}{2}\frac{\widehat{L_{ij}M_{ij}}}{\widehat{M_{ij}M_{ij}}}, \tag{6}$$

$$L_{ij} = \widehat{\bar{u}_i\bar{u}_j} + \widehat{\bar{u}}_i\widehat{\bar{u}}_j, \tag{7}$$

$$M_{ij} = \Delta^2\widehat{\bar{S}\bar{S}_{ij}} + \widehat{\Delta^2\bar{S}}\,\widehat{\bar{S}}_{ij}, \tag{8}$$

where $\widehat{(\,)}$ indicates the averaging over the cell faces, $\widetilde{(\,)}$ indicates the second filtering operation, and $\widetilde{\Delta} = 2\Delta$ is the second filter length. Finally, the filtered Lorentz force in the extended momentum equation is calculated as

$$\bar{F}_i^L = \epsilon_{ijk}\bar{J}_j\bar{B}_k, \tag{9}$$

where $\bar{J}_i$ is the filtered total current density and $\bar{B}_k$ is the filtered magnetic field. In the present study, we are dealing with the highly electrically conducting fluid (liquid metal) implying that the induced magnetic field can be neglected. Consequently, the one-way MHD coupling approach for the moving electrically conducting fluid can be formulated as

$$Re_m = \frac{u_0 D}{\lambda} \ll 1, \tag{10}$$

$$\bar{J}_i = \sigma\left(-\frac{\partial\bar{\phi}}{\partial x_i} + \epsilon_{ijk}\bar{u}_j\bar{B}_k\right), \tag{11}$$

where Re_m is the magnetic Reynolds number, u_0 is the inlet bulk velocity, D is the characteristic length, λ is the magnetic diffusivity, σ is the electrical conductivity of the fluid, J_i is the total current density, and ϕ is the electric potential. To find the electric potential, the Poisson equation, obtained by substituting the zero-divergence total current density condition into Eq. (11), is used:

$$\frac{\partial^2\bar{\phi}}{\partial x_i^2} = \frac{\partial}{\partial x_i}(\epsilon_{ijk}\bar{u}_j\bar{B}_k). \tag{12}$$

Finally, to define the flow regimes, the following non-dimensional numbers need to be introduced:

$$Re = \frac{u_0 D}{\nu}, \quad Ha = BD\sqrt{\frac{\sigma}{\rho\nu}}, \tag{13}$$

where Re is the Reynolds number and Ha is the Hartmann number.

B. Arbitrary electrically conductive walls

Continuous contact of a moving electrically conductive fluid subjected to an external magnetic field, with surrounding electrically conductive walls, leads to the transfer of the electric current density between the fluid/wall interface. To model this phenomenon, we have applied our recently developed conjugated MHD method[39] based on splitting the computation domain into liquid and solid sub-domains. Consequently, the Poisson equation is solved separately for each sub-domain as

$$\frac{\partial}{\partial x_i}\left(\sigma_L\frac{\partial\bar{\phi}_L}{\partial x_i}\right) = \frac{\partial}{\partial x_i}(\epsilon_{ijk}\sigma_L\bar{u}_j\bar{B}_k), \tag{14}$$

$$\frac{\partial}{\partial x_i}\left(\sigma_S\frac{\partial\bar{\phi}_S}{\partial x_i}\right) = 0, \tag{15}$$

where subscript L marks the liquid sub-domain values and S marks the solid sub-domain values. In order to characterize the flow regimes with electrically conductive walls, we introduce the following wall conductivity ratio parameter:

$$C_d = \frac{\sigma_S d_w}{\sigma_L D}, \tag{16}$$

where d_w is the characteristic thickness of the wall.

C. Numerical details

The discretized forms of the above-listed transport equations [Eqs. (3)–12)] were solved by our in-house finite-volume code[39] based on the open-source library OpenFOAM.[40] The calculation of the Lorentz force is based on the Four Steps Projection Method,[41] which fulfills the zero-divergence condition of the total electric current density on all cell faces. The second-order central differencing scheme (CDS) was used for spatial discretization, and the second-order backward scheme was used for temporal discretization. To obtain the electric potential values at the interface between the solid and fluid sub-domains, the weighted-flux scheme was applied.[42] Finally, coupling between the velocity and pressure fields was established through the PISO algorithm.[43]

III. GEOMETRY AND FLOW REGIMES

A. Geometry and mesh

The entire computational domain consists of two main parts: (i) the long square duct representing the liquid metal sub-domain and (ii) two arbitrary conductive finite walls representing the solid sub-domain (Fig. 1). The width of the square duct is D, the thickness of the conductive wall is d_w, and the length of the entire domain is L. It should be noted that special attention should be devoted to the length of the domain in terms of proper capturing of the coexisting laminar and turbulence regions (so-called patterned turbulence[11]) and therefore, the specific length of $L = 40D$ was chosen. To carry out the simulations,

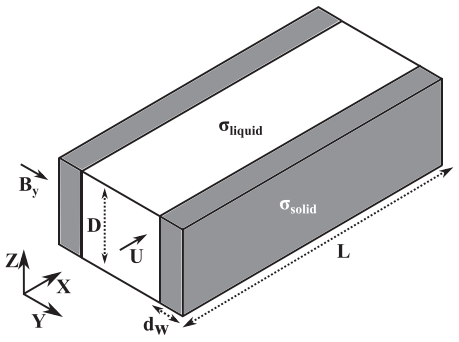

FIG. 1. Sketch of the computational domain (not to scale). The gray color indicates finite arbitrary conductive walls (solid domain), while the white color indicates the liquid domain.

the orthogonal hexahedral non-uniform mesh was created. The numerical mesh was split into two sub-domains with the following distribution of control volumes: $(N_x \times N_y \times N_z = 720 \times 80 \times 80)_{liquid}$ and $(N_x \times N_y \times N_z = 720 \times 12 \times 80)_{solid}$, respectively. The mesh was created in a such way to ensure the continuity of grid lines between the sub-domains. To exclude numerical errors on the interface between solid and liquid regions, the size of the first cells on each side was equal. Additional mesh requirement is associated with the proper numerical resolving of the Hartmann (walls perpendicular to the imposed magnetic field) and Shercliff (walls aligned with the imposed magnetic field) boundary layers. The mesh was refined in the boundary layers with the following set of the non-dimensional wall-distance parameters: $\Delta y^+_{wall} = 0.77$ and $\Delta z^+_{wall} = 0.79$. Such a refinement corresponds to approximately nine mesh points for the Hartmann layer and over 20 mesh points for the Shercliff layer. The coarser mesh was applied in the core region with the following set of the parameters: $\Delta y^+_{core} = 11$ and $\Delta z^+_{core} = 10.7$. A cell-to-cell expansion ratio of $k_{\exp} \approx 1.05$ was used in the y- and z-directions. An uniform mesh distribution was imposed in the streamwise x-direction with $\Delta x^+ = 21$. The mesh accuracy was evaluated via the resolution criteria $K = k_{res}/(k_{res} + k_{sgs})$, where k_{res} is the resolved turbulent kinetic energy and k_{sgs} is the sub-grid scale turbulent kinetic energy. In the close proximity of the wall, the resolution criteria $K \approx 0.88$. In the rest of the computational domain $K \approx 0.96$. According to Pope and Pope,[44] the present values of the resolution criteria and Δ^+ correspond to the well-resolved LES.

B. Boundary conditions and flow regimes

The turbulent flow of the liquid metal is continuously driven in the x-direction by the pressure gradient. In order to maintain turbulence in the duct, periodic boundary conditions were imposed at the inlet and outlet of the duct. All other surfaces act as walls with no-slip velocity boundary conditions. The external constant uniform magnetic field is aligned with the y-direction (Fig. 1). The arbitrary electrically conductive finite walls are placed perpendicular to the imposed magnetic field (Hartmann walls). The top and bottom walls parallel to the magnetic field (Shercliff walls) were kept as fully electrically insulated $[(\partial\phi)/(\partial n) = 0$ and $C_d = 0]$. The used arrangement of the conductive and insulated walls was theoretically postulated to be able to potentially impose significant changes on flow and turbulence reorganization.[12]

To focus primarily on the wall conductivity effects, the Reynolds and Hartmann number were fixed, $Re = 5602$ and $Ha = 21.2$. This set of the non-dimensional parameters proved to be sufficient to impose a significant flow and turbulence reorganization of the initially fully developed turbulence when all duct walls were electrically insulated.[21] We have considered a wide range of the wall conductivity parameter (C_d), ranging from the fully electrically insulated to fully electrically conducting, i.e., $0 \le C_d \le \infty$. For the asymptotic wall conductivities, the solid sub-domains can be excluded. The additional neutral case at $Ha = 0$ was also considered for validation purposes. An overview of all performed simulations is presented in Table I. To obtain fully convergent first- and second-moments statistics, we have used a time-averaging period of 300 flow-through times.

TABLE I. The overview of the flow conditions simulated in the present work.

Re	Ha	C_d, Hartmann walls
5602	0	...
	21.2	0
		0.05
		0.1
		0.15
		0.25
		0.5
		5
		∞

IV. RESULTS AND DISCUSSION

A. Reorganization in the flow structure

We start our analysis by showing the instantaneous flow features (arbitrary time) in the forms of the iso-surfaces of the second invariant of the velocity gradient tensor (Q-criterion), Fig. 2. It can be seen that a dense pattern is observed for the pure hydrodynamic case ($Ha = 0$), Fig. 2(a). Activation of the magnetic field for the electrically perfectly insulated walls ($C_d = 0$) leads to a suppression of coherent structures in the proximity of the Hartmann walls and in the duct center, Fig. 2(b). The distribution of coherent structures near the top Shercliff wall shows localized turbulent puffs, which are the first indicators of the patterned turbulence formation. The presence of these puffs is expected because of the present value of $Re/Ha = 264$ being close to the approximate transition limit of $Re/Ha = 250$ determined by Zikanov *et al.*[11] for the patterned MHD turbulence.

With the activation of the finite electrical conductivity of the Hartmann walls, even relatively low value of the conductivity ratio parameter ($C_d = 0.05$) produced a significant turbulence suppression, Fig. 2(c). Now, the coherent structures are less dense in the vicinity of the Shercliff walls and almost vanished near the Hartmann walls. Moreover, in contrast to the case of the fully electrically insulated walls ($C_d = 0$), the clustering of turbulent puffs near the Shercliff walls is more pronounced. This behavior is further enhanced at $C_d = 0.1$, where distinct morphology of laminar and turbulent spots can be observed, Fig. 2(d). The full laminarization occurs at $C_d = 0.15$, Fig. 2(e). The here observed patterned turbulence phenomenon is a well-recognized feature of the characteristics turbulent to laminar suppression of the MHD turbulence, as previously reported.[11,23] However, the appearance of this regime was always associated with a continuous increase in the magnetic field strength but not with the fixed Ha and variable C_d. The onset of patterned turbulence is sensitive to the length of the computational domain (required to be at least eighty half-widths of the duct, as shown by Krasnov *et al.*[23]) A significantly reduced horizontal extension of the computational domain can artificially suppress the turbulent puffs producing a fully laminarized flow regime. To be able to properly resolve the coexistence of the laminar/turbulent flow regimes within the duct, the length of the square duct was selected to satisfy this condition, i.e., $L = 40D$. With a further increase in $C_d = 0.25$, the turbulent puffs reappear, as shown in Fig. 2(f). This turbulence regeneration process is characterized by the appearance of clusters of turbulence puffs in the duct center. At $C_d = 0.5$, the clusters of turbulent puffs expand toward the Hartmann walls, Fig. 2(g). After reaching $C_d = 5$, the coherent structures are significantly denser than for the case of the electrically insulated walls ($C_d = 0$), as it can be seen in Fig. 2(h). Finally, when $C_d \to \infty$, the

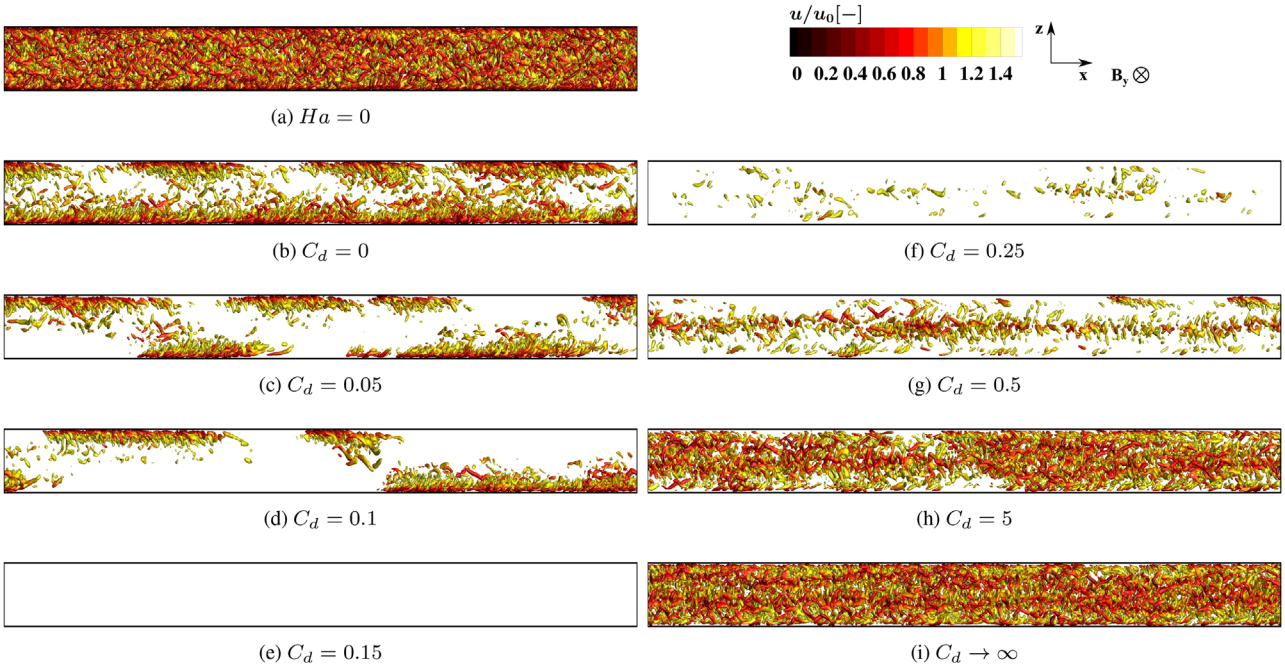

FIG. 2. The side-view of the iso-surfaces of the second-invariant of the velocity gradient (Q-criterion, $Q = 0.8\ s^{-2}$) colored by instantaneous non-dimensional velocity magnitude ($|u|/u_0$) at (a) $Ha = 0$, and (b)–(i) $Ha = 21.2$, $0 \leq C_d < \infty$. Note that the scale factor of $L_{scale} = 0.4$ is applied in the x-direction for a better visibility.

turbulence state is fully recovered portraying a very dense distribution of coherent structures, Fig. 2(i).

Next, we focus on the long-term time-averaged flow characteristics. The contours of the mean velocity magnitude spatially averaged over the entire duct length, for different values of C_d, are shown in Fig. 3. The velocity distribution for the MHD neutral case exhibits a fully symmetrical pattern with the maximum value in the duct center, Fig. 3(a). Activation of the magnetic field for the duct with electrically insulated walls ($C_d = 0$) produced elongation of the mean velocity magnitude toward the Shercliff walls, Fig. 3(b). By replacing the electrically insulated Hartmann walls with the weekly conducting ones ($C_d = 0.05$), further elongation of the high-velocity region toward the Shercliff walls and further reduction from the Hartmann walls was obtained, Fig. 3(c). At $C_d = 0.15$, an interesting flow reorganization occurred, Fig. 3(d). It can be seen that the two distinct regions with elevated velocity magnitude were generated in the proximity of Shercliff walls. This distribution is a consequence of the flow laminarization, as previously illustrated in Fig. 2(d). When a partial regeneration of the turbulence was obtained at $C_d = 0.25$, the wall jets in the proximity of Hartmann walls start to be elongated in the y-direction, forming two distinct ellipsoid-like regions, Fig. 3(e). For $C_d = 0.5$, a further reduction of these distinct wall jet regions is obtained, Fig. 3(f). From $C_d = 5$ to $C_d \to \infty$, just marginal changes can be observed, indicating the saturation regime was achieved already at the previous value of C_d, Figs. 3(g) and 3(h).

It is interesting to note that the previous studies dealing with laminar MHD flows and electrically conductive walls demonstrated a gradual change of the velocity pattern with an increase in the wall conductivity.[28,29,39] In the laminar MHD duct flows, there were no sudden transitions occurring between $C_d = 0.05$, $C_d = 0.15$, and $C_d = 0.25$. Here, we postulate that observed non-monotonic behavior of the mean velocity magnitude are the consequence of the initial re-laminarization and re-appearance of the turbulence in the duct. To confirm this, we have evaluated the profiles of the non-dimensional mean streamwise velocity along the central vertical (between Shercliff walls) and horizontal (between Hartmann walls) cross sections, Fig. 4. The DNS results of[45] for the non-MHD case ($Ha = 0$) in the square duct flow were used as a reference for validation of our simulations. It can be seen that good agreement was obtained for the reference case. With changes in the electrical conductivity of the side walls, significant deviations from the classic log-law distribution were obtained in the vertical cross section, Fig. 4(a). Already at $C_d = 0$ and $C_d = 0.05$, the vertical profiles exhibited re-laminarization trends. The laminarized state was obtained at $C_d = 0.15$. After this point, a further increase in C_d reversed this behavior, resulting in distributions closer to the neutral log-law behavior, confirming the turbulence re-appearance. The horizontal profiles (i.e., between the Hartmann walls) were showing much less variation, Fig. 4(b). Even for the $C_d = 0.15$ value, the deviation from the characteristic log-law distribution was just marginal.

Effects of the wall conductivity on the secondary motion (long-term time-averaged and spatially averaged y- and z-velocity components) are shown in Fig. 5. For the MHD neutral case, a full diagonal symmetrical distribution was generated with eight identical size eddies, Fig. 5(a). This diagonal symmetry was broken with the activation of the magnetic field for the case where all walls were electrically insulated ($C_d = 0$), Fig. 5(b). The eddies in the proximity of Shercliff walls were suppressed, while the eddies in the proximity of the Hartmann walls got elongated in the y-direction. By replacing the electrically

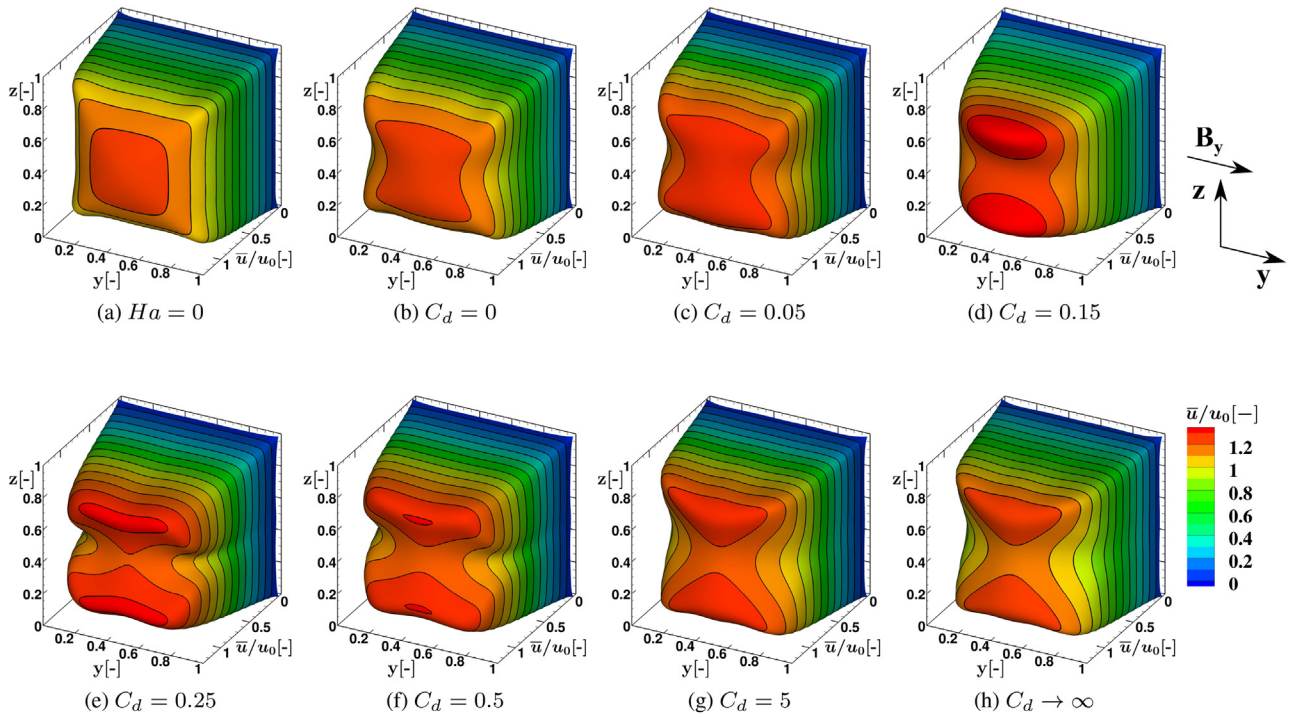

FIG. 3. The time- and spatially averaged (along the entire duct length) non-dimensional velocity magnitude distribution in the vertical cross section: (a) $Ha = 0$, and (b)–(h) $Ha = 21.2$, $0 \le C_d < \infty$.

insulated with electrically conducting walls (i.e., $C_d = 0.05$), the eddies located near the Shercliff walls slightly expanded, Fig. 5(c). For $C_d = 0.15$, because of a sudden flow re-laminarization, there were no secondary motions generated, Fig. 5(d). With further increase in C_d ($0.25 \le C_d \le 0.5$) and turbulence regeneration, the secondary flow patterns reappeared, Figs. 5(e)–5(h). Now, the eddies are differently organized, and the diagonal symmetry was replaced by the central vertical line symmetry. For $C_d = 0.25$ and 0.5, the eddies are oriented in the direction of the imposed magnetic field (i.e., the y-direction), Figs. 5(e) and 5(f). With a further increase in the wall conductivity, the eddies in the proximity of the Shercliff walls were suppressing the ones along the Hartmann walls, Fig. 5(g). Again, the condition of the perfectly conducting walls just marginally changed the morphology of secondary motion eddies, Fig. 5(h).

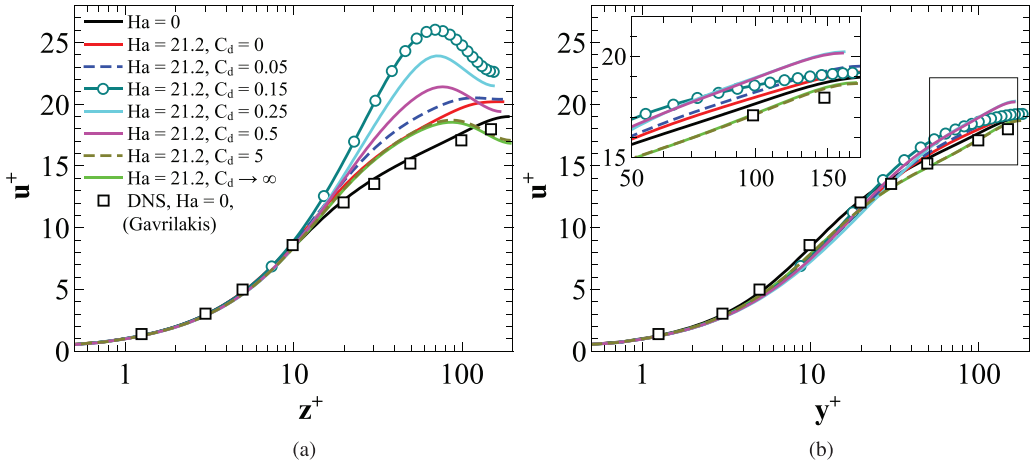

FIG. 4. Dependency of the time-averaged non-dimensional streamwise velocity $u^+ = u/u_\tau$ vs the non-dimensional wall distance $[y, z]^+ = u_\tau[y, z]/\nu$ along the central vertical (between the Shercliff walls) (a) and horizontal (between the Hartmann walls) (b) cross sections.

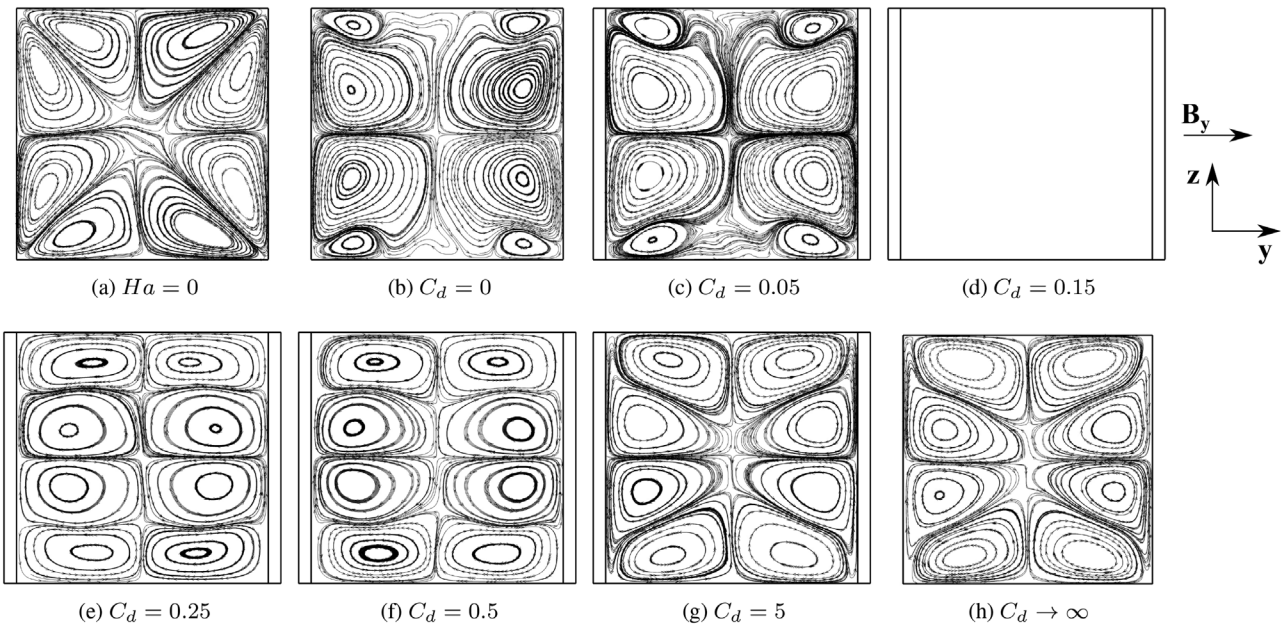

FIG. 5. The time-averaged two-dimensional (y- and z-components) velocity streamlines indicating the secondary motions in the vertical (the x-component) cross-section at (a) $Ha = 0$, and (b)–(h) $Ha = 21.2$, $0 \leq C_d < \infty$.

To provide detailed insights into the origins of the flow reorganization, we focus on distributions of the electromagnetic parameters. The contours of the mean electric potential with superimposed streamlines of the total current density are plotted in Fig. 6. By evaluating the case of the fully electrically insulated walls, it can be seen that a linear distribution between the Shercliff walls is obtained with fully closed loops of the total current density within the fluid region, Fig. 6(b). Activation of the electrically conducting walls leads to a gradual reduction of the local maximum/minimum electric potential zones near the Shercliff walls, Figs. 6(c)–6(h). Furthermore, the loops of the

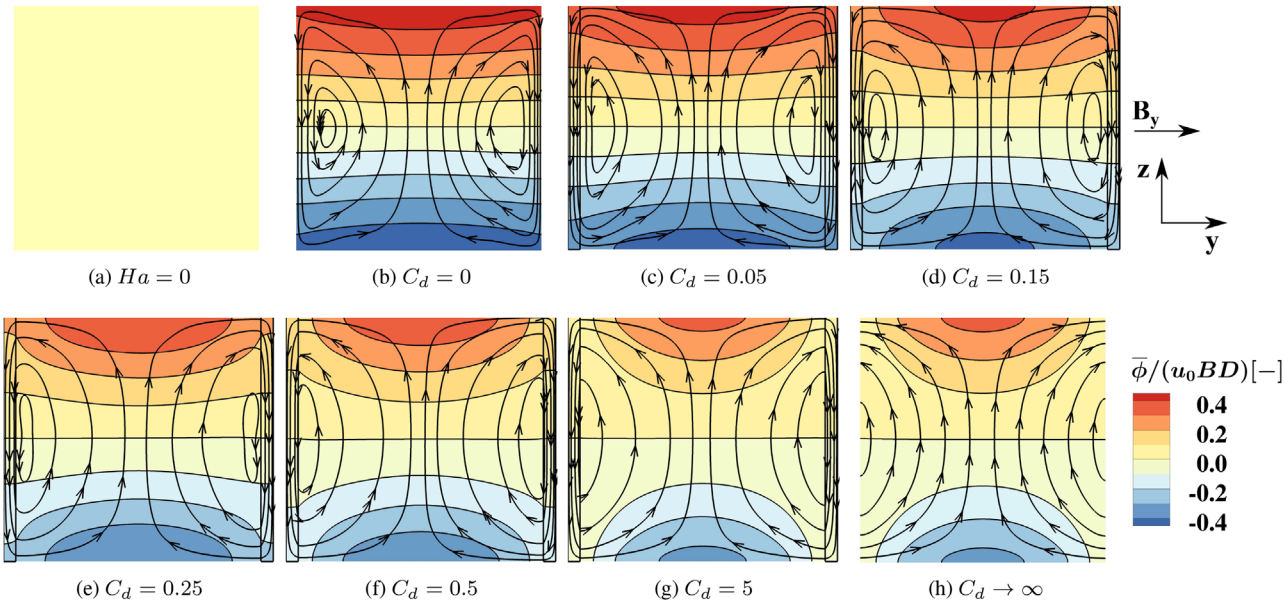

FIG. 6. The contours of the time-averaged non-dimensional electric potential superimposed with the total current density streamlines in the vertical (the x-component) cross-section at (a) $Ha = 0$, and (b)–(h) $Ha = 21.2$, $0 \leq C_d < \infty$.

total current density also penetrate the solid domains. With a C_d increase, the resistance to the current transfer within the walls is significantly reduced, resulting in the gradual changes of the current density loops in the proximity of the Hartmann walls. These changes in the current density behavior immediately contribute to the Lorentz force distribution, as shown in Fig. 7. For the $C_d = 0$ case, the contours of the most dominant streamwise component of the Lorentz force show high positive contributions in the proximity of the Hartmann walls, Fig. 7(b). Further away from the walls, the streamwise component of the Lorentz force becomes negative. The regions near the Shercliff walls are less affected since the direction of the current density is mainly parallel to the imposed magnetic field. An increase in the Hartmann walls conductivity ($0.05 \leq C_d \leq 0.5$) leads to the significant reduction of regions with positive values and appearance of strongly negative regions in the duct center, Figs. 7(c)–7(f). For $C_d = 5$ and $C_d \to \infty$, these high positive regions along the Hartmann walls have disappeared, and a large region with the strong negative contributions is present in the large portion of the duct center, Figs. 7(g) and 7(h).

B. The impact on the turbulence features

Next, we focus on the turbulence parameters. The contours of the long-term time-averaged and spatially averaged (in the streamwise direction) resolved turbulent kinetic energy in the vertical cross-section are shown in Fig. 8. The typical fully symmetrical distribution with enhanced turbulence region in the proximity of walls was obtained for the neutral case, Fig. 8(a). With the MHD activation, for the $C_d = 0$ case, a strong suppression is obtained in the proximity of the Hartmann walls, whereas the suppression in the proximity of the Shercliff walls was less, Fig. 8(b). With a further increase in the $C_d = 0.05$, the turbulence suppression continued, making both the wall and center of duct regions less turbulent, Fig. 8(c). For $C_d = 0.15$ a full flow relaminarization occurred, Fig. 8(d). An interesting distribution of the resolved turbulent kinetic energy was obtained for $C_d = 0.25$, Fig. 8(e). The localized spots placed at approximately halfway between the walls and the duct center can be seen, confirming the localized turbulence regeneration. For $C_d = 0.5$, these localized turbulence regions expanded further, now covering the entire duct center region too, Fig. 8(f). At $C_d = 5$, this process of the turbulence regeneration continued with locally enhanced spots in the proximity of walls, Fig. 8(g). Now, in contrast to the relaminarization process, the regions in the proximity of the Hartmann walls were significantly more turbulent compared to the regions in the proximity of the Shercliff walls. The identical trend with marginal modification was also present at $C_d \to \infty$, confirming the turbulence sustenance, Fig. 8(h). The recovery of the turbulence is correlated with the Lorentz force redistribution and its impact on the flow: two jets directly contribute to the turbulence level in the proximity of the Shercliff walls, while the excessively strong Lorentz force augments the velocity gradient in the proximity of the Hartmann walls.

The profiles of the non-dimensional RMS of the velocity component fluctuations along the central vertical and horizontal intersections for different values of C_d are shown in Fig. 9. Note that additional DNS data were also plotted for the non-MHD[45] and the MHD case with $C_d = 0$.[21] It can be seen that good agreement between our LES and DNS data from the literature was obtained. For the RMS profiles for all velocity components along the central vertical line exhibit qualitatively similar behavior: a continuous decrease in the $0 \leq C_d \leq 0.15$ range, a full relaminarization at $C_d = 0.15$, and a continuous increase in the $0.25 \leq C_d < \infty$ range, Figs. 9(a)–9(c). It should be noted that after the turbulence regeneration, the obtained peak RMS value in the wall proximity of all velocity components were smaller than corresponding values for the initial non-MHD case. Furthermore, in this

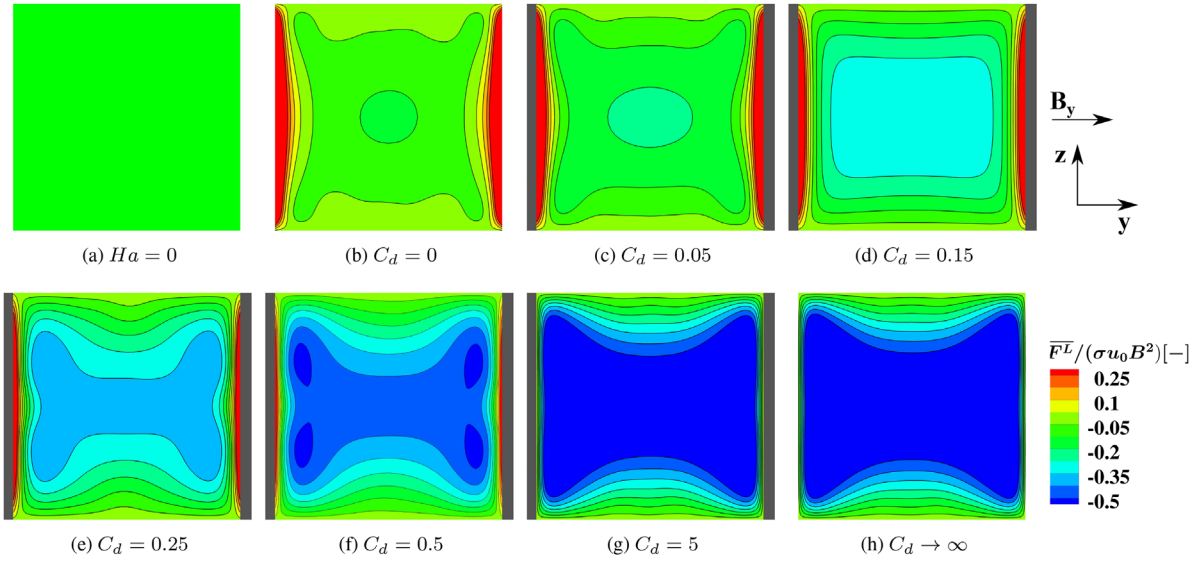

(a) $Ha = 0$ (b) $C_d = 0$ (c) $C_d = 0.05$ (d) $C_d = 0.15$

(e) $C_d = 0.25$ (f) $C_d = 0.5$ (g) $C_d = 5$ (h) $C_d \to \infty$

FIG. 7. The time-averaged non-dimensional streamwise Lorentz force contours in the vertical (the x-component) cross-section at (a) $Ha = 0$, and (b)–(h) $Ha = 21.2$, $0 \leq C_d < \infty$.

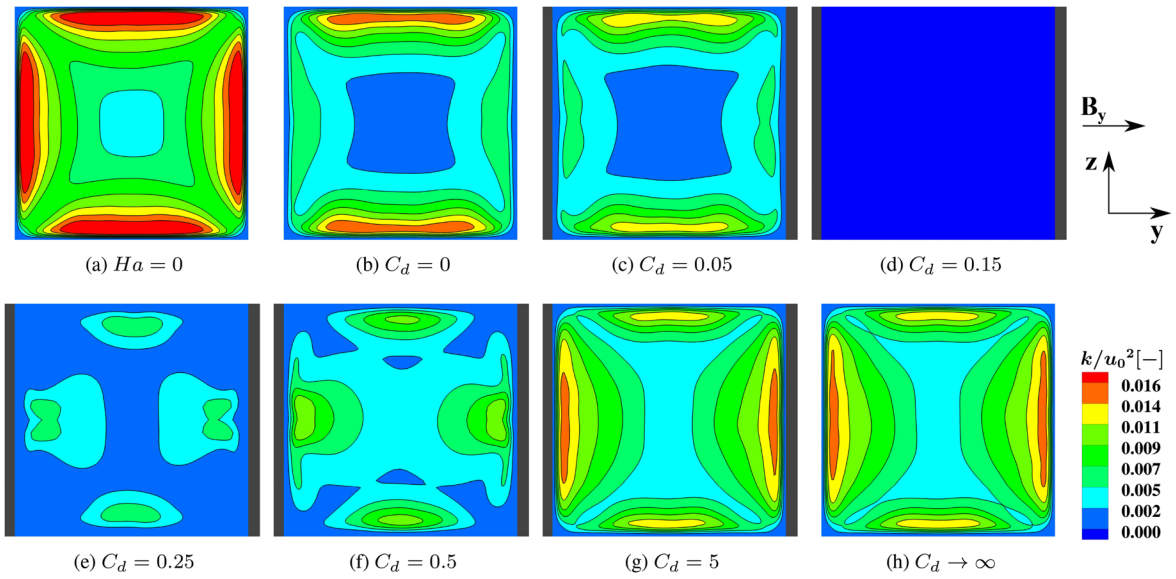

FIG. 8. The resolved non-dimensional turbulent kinetic energy contours in the vertical (the x-component) cross-section at (a) $Ha = 0$, and (b)–(h) $Ha = 21.2$, $0 \leq C_d < \infty$.

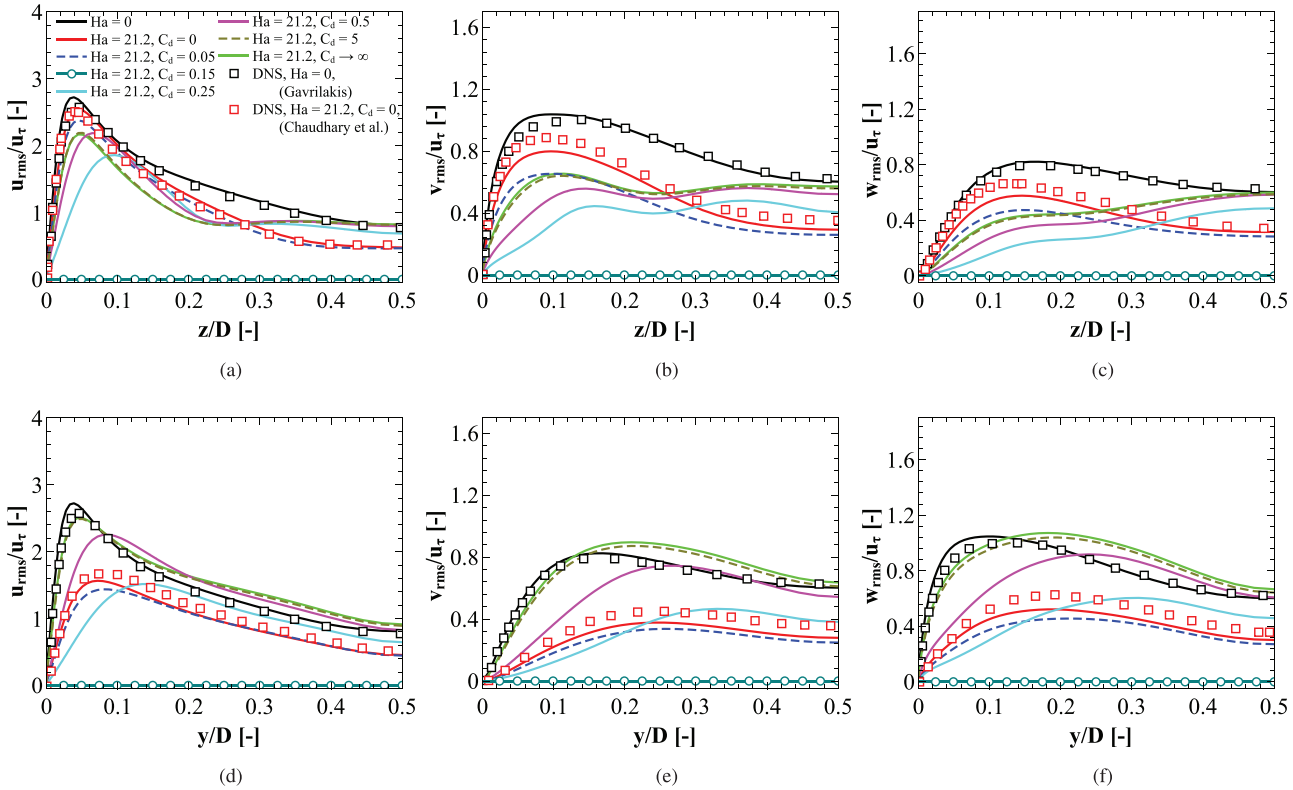

FIG. 9. The profiles of non-dimensional RMS of the velocity fluctuations (u', v', and w') along the central horizontal and vertical intersections in the proximity of the (a)–(c) Shercliff and (d)–(f) Hartmann walls.

turbulence regeneration phase (i.e., for $C_d \geq 0.25$), all RMS profiles along the central vertical line exhibit characteristic double peaks. The second peaks were located close to the duct center are asymptotically approaching the non-MHD values and are higher than the reference MHD case with the fully insulated walls ($C_d = 0$). The profiles of the RMS of the velocity components along the central horizontal line show a different behavior, Figs. 9(d)–9(f). There are no secondary peaks observed, and for $C_d \geq 5$, in comparison to the non-MHD case, all RMS values show higher values in the region between the near-wall peak location and the center of the duct ($0.15 \leq y/D \leq 0.5$).

The profiles of the turbulent shear stress components are shown in Fig. 10. The vertical profiles of the $\langle u'w' \rangle$ component show monotonous damping of the peak values in the proximity of the Shercliff wall until a full relaminarization was obtained ($0 \leq C_d \leq 0.15$), Fig. 10(a). During the turbulence regeneration process, the near-wall peaks gradually increase until the saturation point was reached at $C_d = 5$. Interestingly, during the process of the turbulence reappearance and sustenance ($0.25 \leq C_d \to \infty$), characteristic negative contributions of the shear stress were obtained in the $0.2 \leq z/D \leq 0.5$ region. This behavior of the vertical profiles, as well the double-peak behavior of the v_{rms} and w_{rms} components [already discussed in Figs. 9(b) and 9(c)], can be explained in terms of the double-jet M-shape formation in the proximity of the Shercliff walls, as illustrated in Figs. 3(e)–3(h). The horizontal profiles of the $\langle u'v' \rangle$ turbulent stress component exhibited a qualitatively different behavior, Fig. 10(b). Here, after the initial effective suppression ($0 \leq C_d \leq 0.15$), an effective recovery occurred, resulting in the rapid increase in the shear stress component. Now, the peak values in the wall proximity reached values of the non-MHD case (albeit with their locations moved farther away from the Hartmann wall). Furthermore, the values of the $\langle u'v' \rangle$ were surpassing values for the neutral non-MHD case in ($5 \leq C_d \to \infty$) range.

Next, we move to analyze the budget of the turbulent kinetic energy transport equation. By introducing the long-term time-averaging $\langle\rangle$ and fluctuating ($'$) operators, the equation can be written in the general form as follows:

$$\underbrace{\langle u_j \rangle \frac{\partial k}{\partial x_j}}_{\text{Convection}} = \underbrace{-\langle u_i' u_j' \rangle \frac{\partial \langle u_i \rangle}{\partial x_j}}_{\text{Production}} \underbrace{-\frac{1}{2}\frac{\partial \langle u_i' u_i' u_j' \rangle}{\partial x_j}}_{\text{Turbulent diffusion}} \underbrace{-\frac{1}{\rho}\left\langle u_i' \frac{\partial p'}{\partial x_i} \right\rangle}_{\text{Pressure diffusion}}$$
$$\underbrace{+2\nu \frac{\partial \langle S_{ij}' u_i' \rangle}{\partial x_j}}_{\text{Viscous diffusion}} \underbrace{-2\nu \langle S_{ij}' S_{ij}' \rangle}_{\text{Dissipation}} \underbrace{-\frac{\partial \langle \tau_{ij}^{sgs} u_i' \rangle}{\partial x_j}}_{\text{SGS diffusion}} \underbrace{+\langle \tau_{ij}^{sgs} S_{ij}' \rangle}_{\text{SGS dissipation}}$$
$$\underbrace{-2\frac{\sigma}{\rho} k B_k^2}_{\text{MHD loss}} \underbrace{-\frac{\sigma}{\rho} \epsilon_{ijk} B_k \left\langle u_i' \frac{\partial \phi'}{\partial x_j} \right\rangle + \frac{\sigma}{\rho} \langle u_i' u_j' \rangle B_i B_k}_{\text{MHD gain}}. \quad (17)$$

The distributions of the turbulent kinetic energy budget terms (scaled with u_0^3/D) along the central vertical and horizontal intersections of the central vertical plane are presented in Figs. 11 and 12. This separation of the term contributions is done to provide a better overview of the physical mechanism of the energy distribution. The contributions of the pressure and sub-grid diffusion as well as sub-grid dissipation are not shown due to their negligible contributions compared with the remaining terms. For comparative purposes, we also have plotted budget contributions of the fully insulated case ($C_d = 0$) from the literature.[21] It can be concluded that for all presented budget contributions, in general, good agreement between the present results and results from the literature[21] was obtained. Some minor local differences (e.g., for turbulent diffusion and viscous dissipation) can be explained in terms of different numerical approaches used.

Starting from the mechanical production term, it can be seen that the activation of the imposed magnetic field suppresses the characteristic near-wall peak values in the proximity of both walls until the full relaminarization is achieved ($0 \leq C_d \leq 0.15$), Figs. 11(a) and 11(d). With further increase in C_d, the production contribution increases, the final peak value (at $C_d \to \infty$) in the proximity of the Hartmann wall now exceeds the value in the proximity of the Shercliff wall. When compared to the peak values for the $C_d = 0$ case, the peak value for $C_d \to \infty$ in the proximity of the Hartmann wall shows an increase in

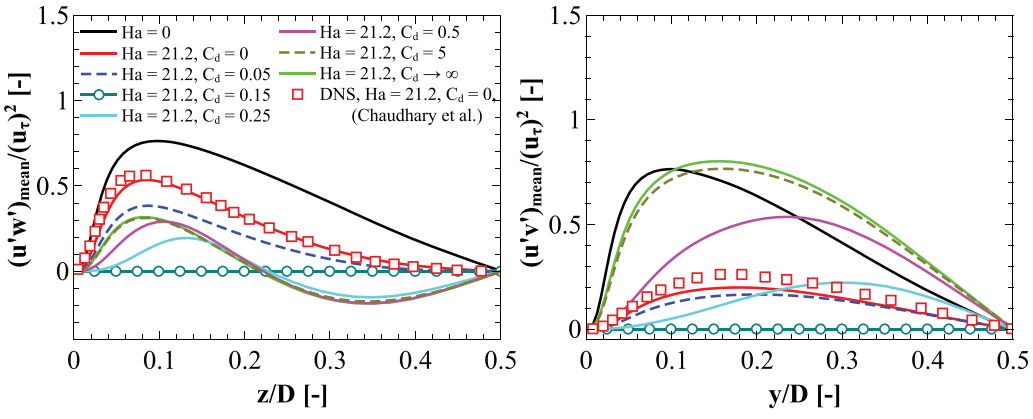

FIG. 10. The non-dimensional time-averaged profiles of non-diagonal components of the Reynolds stress tensor $\overline{u'w'}$ and $\overline{u'v'}$ along the central vertical and horizontal intersections in the proximity of the (a) Shercliff and (b) Hartmann walls.

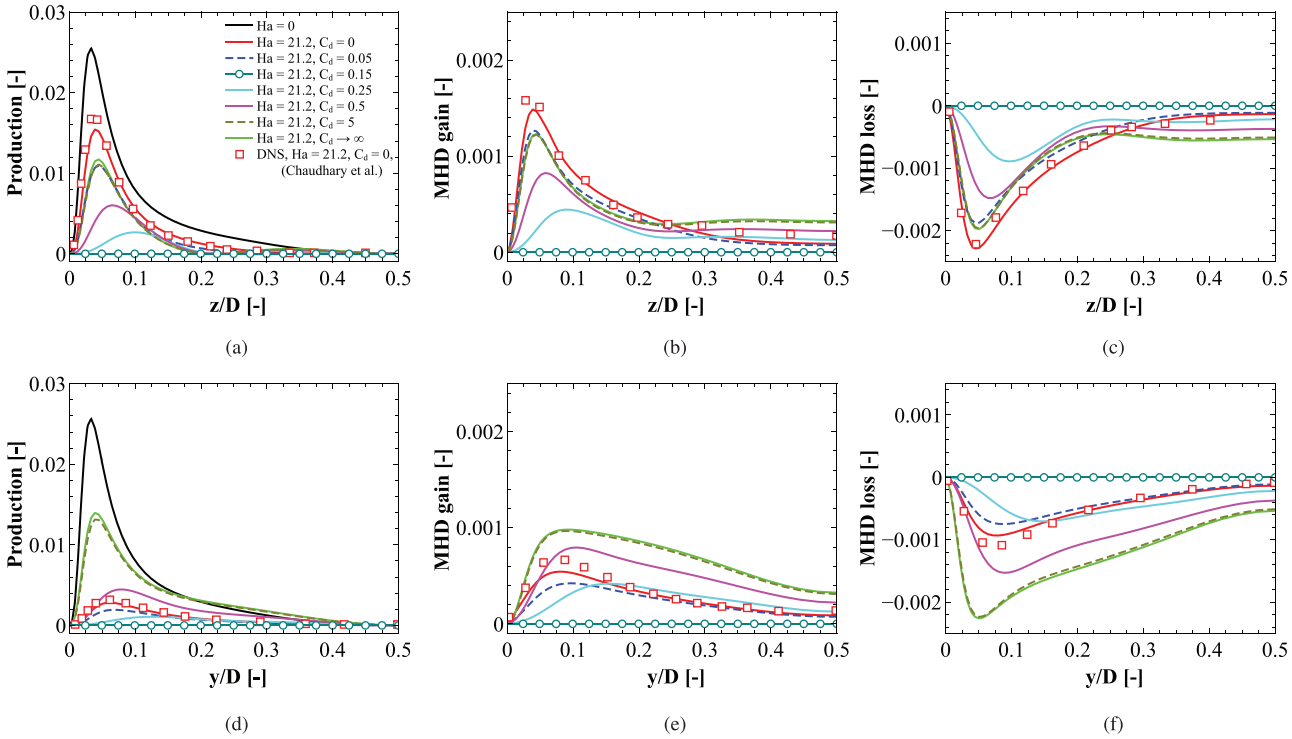

FIG. 11. The profiles of non-dimensional turbulent kinetic energy budget terms (production, MHD gain and MHD loss) extracted along the central vertical and horizontal intersections in the proximity of the (a)–(c) Shercliff and (d)–(f) Hartmann walls.

almost factor four [Fig. 11(d)], whereas the peak value in the proximity of the Shercliff wall was reduced by approximately 60%, Fig. 11(a).

The qualitative similar behavior of the production term is also observed for profiles of the MHD gain [Figs. 11(b) and 11(e)] and MHD loss budget terms [Figs. 11(c) and 11(f)]. However, in contrast to the production term, the MHD budget contributions changed less significantly in response to the varied wall conductivity, especially in the proximity of the Hartmann wall, Fig. 11(e). The peak values of the MHD gain term for $C_d = 5$ and $C_d \to \infty$ in the vicinity of the Hartmann wall are now slightly enhanced (approximately 20%) in comparison to the $C_d = 0$ case. In contrast, the MHD loss term peak in the proximity of the Hartmann wall almost doubled for $C_d \to \infty$ when compared to the $C_d = 0$, Fig. 11(f). By comparing the order of magnitude between the production [Figs. 11(a) and 11(d)] and MHD gain budget [Figs. 11(b) and 11(e)] terms, we can conclude the flow reorganization (because of the presence of the mean velocity gradient in the production term) has a leading role with respect to the pure turbulence contributions and their interaction with the imposed magnetic field. The profiles of the turbulent and viscous diffusion demonstrate significant contributions only in the proximity of the walls, Figs. 12(a), 12(b), 12(d), and 12(e). In the vicinity of the Shercliff wall, the final $C_d \to \infty$ almost halved in comparison to the $C_d = 0$ case, Fig. 12(a). In contrast to that behavior, for identical values of C_d, the profiles of the turbulent diffusion near the Hartmann wall were augmented for a factor three, Fig. 12(d). The qualitative similar trends were observed also for the viscous diffusion terms, Figs. 12(b) and 12(e). Finally, the dissipation profiles in the proximity of the Shercliff wall show lower values for $C_d \to \infty$ than for $C_d = 0$ case, Fig. 12(c). In contrast, a significant augmentation was obtained in the vicinity of the Hartmann wall for $C_d \to \infty$, Fig. 12(f). This behavior was expected due to a balance between the viscous diffusion and dissipation budget terms at the duct walls.

Next, we analyze the turbulence anisotropy states by plotting the Lumley's turbulence triangles[46] for the turbulent stress components extracted along the central vertical and horizontal intersections, Figs. 13(a) and 13(c), respectively. Here, ξ and η are the second and third-invariants of the anisotropy tensor b_{ij}, defined as

$$6\eta^2 = b_{ij}b_{ji}, \quad 6\xi^3 = b_{ij}b_{jk}b_{ki}, \quad b_{ij} = \frac{\overline{u_i'u_j'}}{2k} - \frac{1}{3}\delta_{ij}. \tag{18}$$

Starting from the entire map of turbulence state distributions for the neutral (non-MHD) case, one can observe typical two-component (2C) region close to the walls, followed by the one-component (1C) state, and the final axisymmetric state (AX), Figs. 13(a) and 13(c). Then, to provide a better insight into turbulence state reorganization caused by the imposed electrical conductivity of the duct side walls, we provide zoom-ins in the proximity of the one-component turbulence state point (1C) for profiles extracted along the vertical and horizontal central intersections, respectively, as shown in Figs. 13(b) and 13(d).

The minimum of the turbulence anisotropy (defined in terms of the farthest distance from the 1C limit point) was obtained for $Ha = 0$ case for both walls. In the vicinity of the Shercliff wall, an increase in the electrical wall conductivity leads to the anisotropy increase in $0 \leq C_d < 0.25$ range, Fig. 13(b). The peak is achieved at $C_d = 0.25$

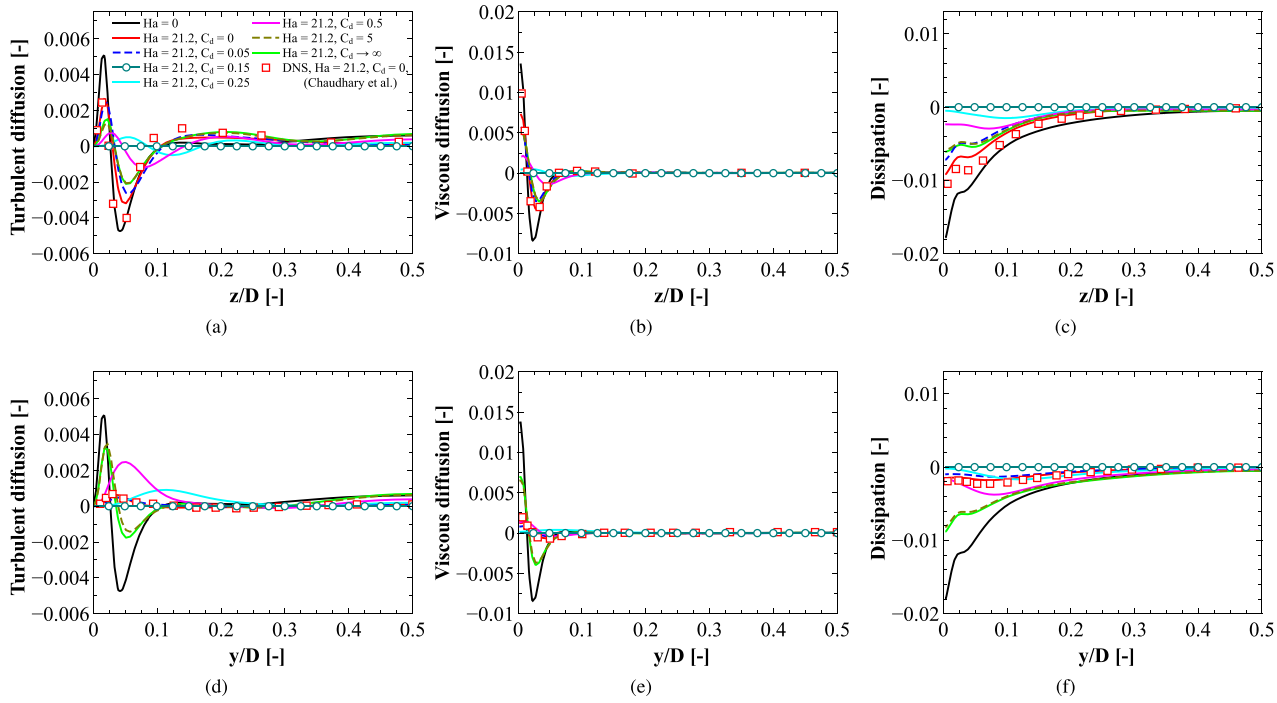

FIG. 12. The profiles of the non-dimensional turbulent kinetic energy budget terms (turbulent diffusion, viscous diffusion and dissipation) along the central vertical and horizontal intersections in the proximity of the (a)–(c) Shercliff and (d)–(f) Hartmann walls.

after which a decrease is obtained in $0.25 < C_d < \infty$ range. Despite this reduction in the turbulence anisotropy, the final $C_d \to \infty$ value is still more anisotropic than the $C_d = 0$ situation. The turbulence anisotropy in the proximity of the Hartmann wall showed a different behavior, Fig. 13(d). Now, an enhancement of turbulence anisotropy was observed only in the relatively narrow region $0 \leq C_d < 0.05$. At $C_d = 0.05$, the peak value was reached, followed by a gradual decrease as C_d increased. In contrast to the Shercliff wall, the anisotropy value in the vicinity of the Hartmann wall at $C_d \to \infty$ is much closer to the neutral case ($Ha = 0$) value.

Finally, we performed the analysis of the time series of the instantaneous streamwise velocity sampled at characteristic monitoring locations in the duct center and in proximities of the Shercliff and Hartmann walls for different values of the C_d, Fig. 14. It can be seen that the instantaneous behavior in the duct center is just slightly affected by imposed changes of the C_d parameter, Fig. 14(a). The instantaneous response is different for the near-wall locations, Figs. 14(b) and 14(c). Here, the imprints of the patterned turbulence structures are particularly visible in the form of quasi-periodic signals for the $C_d = 0.1$ case. Corresponding power spectra density (PSD) distributions[47] are shown in Fig. 15. The characteristic slopes of $-5/3$ (Kolmogorov inertial range) and $-16/3$ (dissipation range) do not show any significant changes with imposed C_d variation in the duct center, Fig. 15(a). A sudden appearance of the leading frequency $f = 0.02$ Hz can be seen for $C_d = 0.1$, which corresponds to the characteristic quasi-periodic signal shown in Fig. 14(a). At the location in the proximity of the Shercliff wall, notable differences are obtained for the $C_d = 0.25$, where the inertial range started at the lower frequencies, and where the dissipative range slope becomes less steep, Fig. 15(b). In the vicinity of the Hartmann wall, the observed changes in characteristic slopes were more pronounced, Fig. 15(c). The inertial range started at lower frequencies already at $C_d = 0$, while the dissipation range slope was less rapid at $C_d = 0.1$. With a further increase in C_d, the slope of $-16/3$ in the dissipation range was recovered.

V. SUMMARY AND CONCLUSION

We have performed a numerical study of the turbulent magnetohydrodynamic square duct flow with arbitrary electrically conducting Hartmann walls subjected to a transverse uniform magnetic field. We have assumed the one-way coupling between the fluid flow and imposed magnetic field, and have applied Large Eddy Simulation with the dynamic Smagorinsky sub-grid closure to account for the turbulence. We have varied the typical wall conductance ratio over a wide range of $0 \leq C_d \to \infty$, for fixed values of the Reynolds ($Re = 5602$) and Hartmann ($Ha = 21.2$) numbers (both selected to provide a fully developed turbulence regime). The variation of the electrical conductance of the Hartmann walls has introduced significant flow and turbulence reorganization, which can be classified into the following three stages. The first stage corresponds to the $0 \leq C_d < 0.15$ range, and was characterized by a gradual suppression of the velocity fluctuations and appearance of the patterned turbulence clusters in the vicinity of the Shercliff walls. The second stage was obtained at $C_d = 0.15$, when a full flow laminarization occurred. The final third stage was obtained in the $0.15 < C_d \to \infty$ range, when a turbulence

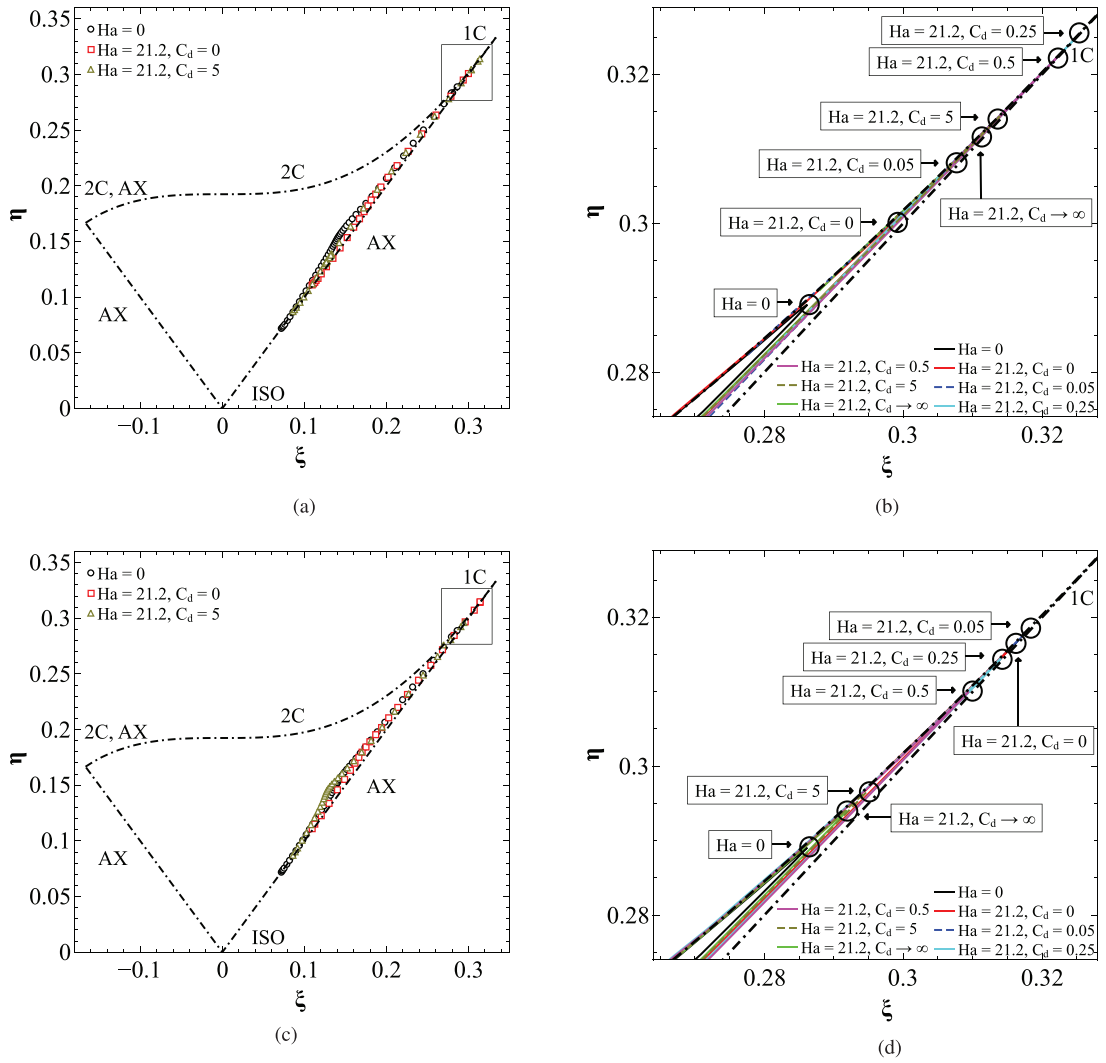

FIG. 13. The anisotropy distribution of the turbulence (Lumley triangle) extracted along the central vertical (in the proximity of the Shercliff wall) (a) and horizontal (in the proximity of the Hartmann wall) (c) profiles of the vertical cross-section of the duct. The zoom-in of the zone indicating one-component turbulence for the Shercliff and Hartmann regions is presented in (b) and (d) correspondingly. The following notation is used for the turbulence states: ISO, isotropic; 2C, two-component; 1C, one-component; AX, axisymmetric.

regeneration (triggered in the regions between the Hartmann walls and the duct center) and sustenance was observed.

The flow morphology, including the secondary flow patterns, went through significant alternation along all three stages. The analysis of the turbulent kinetic energy budgets have provided detailed insight into mechanisms behind the MHD induced flow relaminarization and final turbulence regeneration (i.e., due to the interplay between the flow reorganization and local distribution of the current density). For the perfectly electrically conducting Hartmann walls, the turbulence reached level close to the non-MHD situation (i.e., $Ha = 0$), confirming the full turbulence regeneration after an initial MHD induced suppression. The maximum of the turbulence anisotropy was reached at $C_d = 0.05$ and $C_d = 0.25$ in proximities of the Hartmann and Shercliff walls, respectively. The slopes of the power spectra density distributions were mostly affected in the intermediate range of C_d in the proximity of the Hartmann walls. The provided numerical results also intended to motivate additional experimental studies in the similar range of the Re/Ha working parameters to provide the final answers on turbulence regeneration triggered by the changes of the electrical conductance of the Hartmann walls. The importance of the finite electrical conductance of the Hartmann walls can find direct applications in the flow and turbulence control during the continuous casting and in liquid metal blankets of the new generation of the fusions reactors.

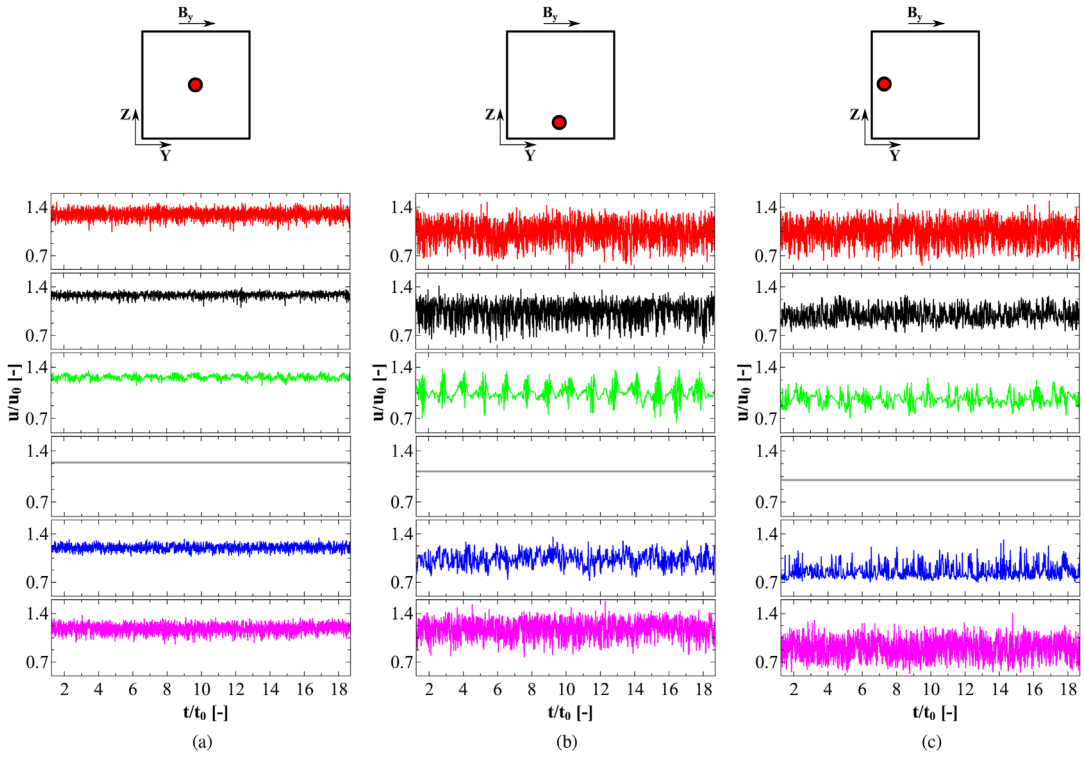

FIG. 14. The time series of the non-dimensional instantaneous streamwise (x-component) velocity in the center of the duct with the following coordinates $p_{yz}(0.5, 0.5)$ (a), in the proximity of the Shercliff wall with the following coordinates $p_{yz}(0.5, 0.1)$ (b), and in the proximity of the Hartmann wall with the following coordinates $p_{yz}(0.1, 0.5)$ (c). The following indication is used: (red line)—$Ha = 0$, (black line)—$Ha = 21.2$, $C_d = 0$, (green line)—$Ha = 21.2$, $C_d = 0.1$, (gray line)—$Ha = 21.2$, $C_d = 0.15$, (blue line)—$Ha = 21.2$, $C_d = 0.25$, (pink line)—$Ha = 21.2$, $C_d \to \infty$.

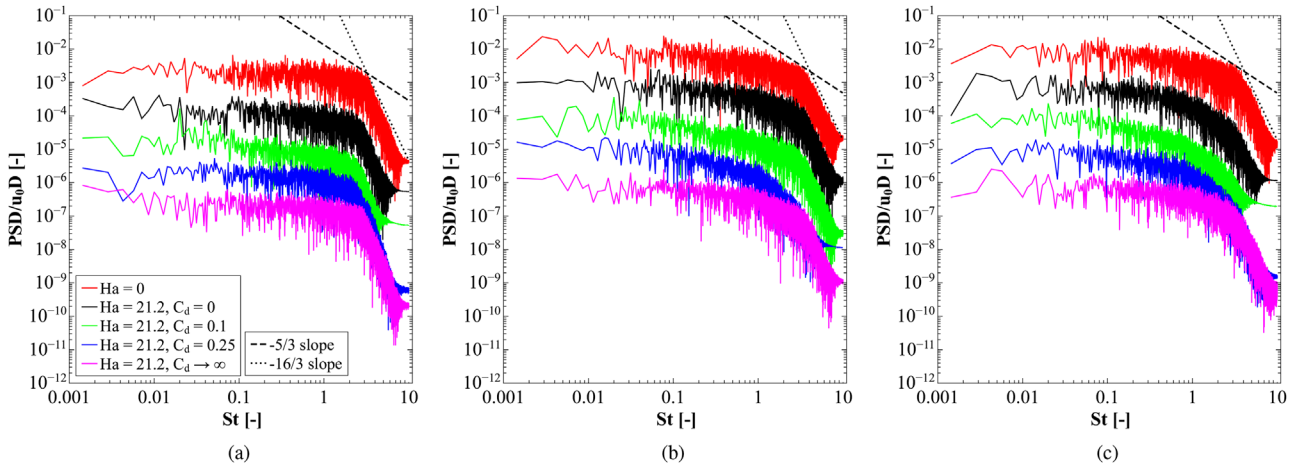

FIG. 15. The power spectral density of the non-dimensional instantaneous streamwise (x-component) velocity for different values of C_d at locations shown in Figs. 14(a)–14(c). Note that due to better visibility, the vertical axis was shifted down for one decade for each consecutive plot.

ACKNOWLEDGMENTS

This project has received funding from the European Union's Horizon 2020 research and innovation program TOMOCON (Smart Tomographic Sensors for Advanced Industrial Process Control) under the Marie Sklodowska-Curie Grant Agreement No.764902.

AUTHOR DECLARATIONS

Conflict of Interest

The authors have no conflicts to disclose.

DATA AVAILABILITY

The data that support the findings of this study are available from the corresponding author upon reasonable request.

REFERENCES

[1]J. Hartmann and F. Lazarus, "Theory of the laminar flow of an electrically conducting liquid in a homogeneous magnetic field," K. Dan. Vidensk. Selsk., Mat. **15**, 1–28 (1937).
[2]H. Alfvén, "Existence of electromagnetic-hydrodynamic waves," Nature **150**, 405–406 (1942).
[3]L. Bühler, "Liquid metal magnetohydrodynamics for fusion blankets," in *Magnetohydrodynamics: Historical Evolution and Trends* (Springer, The Netherlands, 2007), pp. 171–194.
[4]C. Mistrangelo, L. Bühler, C. Koehly, and I. Ricapito, "Magnetohydrodynamic velocity and pressure drop in manifolds of a WCLL TBM," Nucl. Fusion **61**, 096037 (2021).
[5]S. Smolentsev, "Physical background, computations and practical issues of the magnetohydrodynamic pressure drop in a fusion liquid metal blanket," Fluids **6**, 110 (2021).
[6]B. G. Thomas and R. Chaudhary, "State of the art in electromagnetic flow control in continuous casting of steel slabs: Modeling and plant validation," in 6th International Conference on Electromagnetic Processing of Materials EPM (2009); available at http://citeseerx.ist.psu.edu/viewdoc/download?doi=10.1.1.657.5586&rep=rep1&type=pdf.
[7]S.-M. Cho and B. G. Thomas, "Electromagnetic forces in continuous casting of steel slabs," Metals **9**, 471 (2019).
[8]N.-T. Nguyen, "Micro-magnetofluidics: Interactions between magnetism and fluid flow on the microscale," Microfluid. Nanofluid. **12**, 1–16 (2012).
[9]A. Ortiz-Pérez, V. García-Ángel, A. Acuña-Ramírez, L. Vargas-Osuna, J. Pérez-Barrera, and S. Cuevas, "Magnetohydrodynamic flow with slippage in an annular duct for microfluidic applications," Microfluid. Nanofluid. **21**, 138 (2017).
[10]X. Wang, H. Xu, and H. Qi, "Transient magnetohydrodynamic flow and heat transfer of fractional Oldroyd-B fluids in a microchannel with slip boundary condition," Phys. Fluids **32**, 103104 (2020).
[11]O. Zikanov, D. Krasnov, T. Boeck, A. Thess, and M. Rossi, "Laminar-turbulent transition in magnetohydrodynamic duct, pipe, and channel flows," Appl. Mech. Rev. **66**, 030802 (2014).
[12]P. A. Davidson, *An Introduction to Magnetohydrodynamics, Cambridge Texts in Applied Mathematics* (Cambridge University Press, 2001).
[13]S. Kenjereš, "On modeling and eddy-resolving simulations of flow, turbulence, mixing and heat transfer of electrically conducting and magnetizing fluids: A review," Int. J. Heat Fluid Flow **73**, 270–297 (2018).
[14]S. Kenjereš and K. Hanjalić, "On the implementation of effects of Lorentz force in turbulence closure models," Int. J. Heat Fluid Flow **21**, 329–337 (2000).
[15]S. Smolentsev and R. Moreau, "One-equation model for quasi-two-dimensional turbulent magnetohydrodynamic flows," Phys. Fluids **19**, 078101 (2007).
[16]O. Widlund, S. Zahrai, and F. H. Bark, "Development of a Reynolds stress closure for modeling of homogeneous MHD turbulence," Phys. Fluids **10**, 1987–1996 (1998).
[17]X. Miao, K. Timmel, D. Lucas, Z. Ren, S. Eckert, and G. Gerbeth, "Effect of an electromagnetic brake on the turbulent melt flow in a continuous-casting mold," Metall. Mater. Trans. B **43**, 954–972 (2012).
[18]S. Kenjereš, K. Hanjalić, and D. Bal, "A direct-numerical-simulation-based second-moment closure for turbulent magnetohydrodynamic flows," Phys. Fluids **16**, 1229–1241 (2004).
[19]H. Kobayashi, "Large eddy simulation of magnetohydrodynamic turbulent channel flows with local subgrid-scale model based on coherent structures," Phys. Fluids **18**, 045107 (2006).
[20]D. Krasnov, O. Zikanov, J. Schumacher, and T. Boeck, "Magnetohydrodynamic turbulence in a channel with spanwise magnetic field," Phys. Fluids **20**, 095105 (2008).
[21]R. Chaudhary, S. P. Vanka, and B. G. Thomas, "Direct numerical simulations of magnetic field effects on turbulent flow in a square duct," Phys. Fluids **22**, 075102 (2010).
[22]D. Krasnov, O. Zikanov, and T. Boeck, "Numerical study of magnetohydrodynamic duct flow at high Reynolds and Hartmann numbers," J. Fluid Mech. **704**, 421–446 (2012).
[23]D. Krasnov, A. Thess, T. Boeck, Y. Zhao, and O. Zikanov, "Patterned turbulence in liquid metal flow: Computational reconstruction of the Hartmann experiment," Phys. Rev. Lett. **110**, 084501 (2013).
[24]O. Zikanov, D. Krasnov, Y. Li, T. Boeck, and A. Thess, "Patterned turbulence in spatially evolving magnetohydrodynamic duct and pipe flows," Theor. Comput. Fluid Dyn. **28**, 319–334 (2014).
[25]O. Zikanov, D. Krasnov, T. Boeck, and S. Sukoriansky, "Decay of turbulence in a liquid metal duct flow with transverse magnetic field," J. Fluid Mech. **867**, 661–690 (2019).
[26]Y. Yang, W. H. Matthaeus, Y. Shi, M. Wan, and S. Chen, "Compressibility effect on coherent structures, energy transfer, and scaling in magnetohydrodynamic turbulence," Phys. Fluids **29**, 035105 (2017).
[27]A. De Rosis, R. Liu, and A. Revell, "One-stage simplified lattice Boltzmann method for two-and three-dimensional magnetohydrodynamic flows," Phys. Fluids **33**, 085114 (2021).
[28]J. C. R. Hunt, "Magnetohydrodynamic flow in rectangular ducts," J. Fluid Mech. **21**, 577–590 (1965).
[29]A. Sterl, "Numerical simulation of liquid-metal MHD flows in rectangular ducts," J. Fluid Mech. **216**, 161–191 (1990).
[30]T. Arlt, J. Priede, and L. Bühler, "The effect of finite-conductivity Hartmann walls on the linear stability of Hunt's flow," J. Fluid Mech. **822**, 880–891 (2017).
[31]A. Thomas and L. Bühler, "Numerical simulations of time-dependent hunt flows with finite wall conductivity," Magnetohydrodynamics **55**, 319–336 (2019).
[32]L. Bühler, T. Arlt, T. Boeck, L. Braiden, V. Chowdhury, D. Krasnov, C. Mistrangelo, S. Molokov, and J. Priede, "Magnetically induced instabilities in duct flows," IOP Conf. Ser.: Mater. Sci. Eng. **228**, 012003 (2017).
[33]K. Zhang, M. Weeks, and P. Roberts, "Effect of electrically conducting walls on rotating magnetoconvection," Phys. Fluids **16**, 2023–2032 (2004).
[34]A. T. Akinshilo, "Mixed convective heat transfer analysis of MHD fluid flowing through an electrically conducting and non-conducting walls of a vertical micro-channel considering radiation effect," Appl. Therm. Eng. **156**, 506–513 (2019).
[35]A. Blishchik and S. Kenjereš, "Observation of a novel flow regime caused by finite electric wall conductance in an initially turbulent magnetohydrodynamic duct flow," Phys. Rev. E **104**, L013101 (2021).
[36]J. Smagorinsky, "General circulation experiments with the primitive equations: I. the basic experiment," Mon. Weather Rev. **91**, 99–164 (1963).
[37]J. Mao, K. Zhang, and K. Liu, "Comparative study of different subgrid-scale models for large eddy simulations of magnetohydrodynamic turbulent duct flow in OpenFOAM," Comput. Fluids **152**, 195–203 (2017).
[38]D. K. Lilly, "A proposed modification of the Germano subgrid-scale closure method," Phys. Fluids A **4**, 633–635 (1992).
[39]A. Blishchik, M. van der Lans, and S. Kenjereš, "An extensive numerical benchmark of the various magnetohydrodynamic flows," Int. J. Heat Fluid Flow **90**, 108800 (2021).
[40]H. G. Weller, G. Tabor, H. Jasak, and C. Fureby, "A tensorial approach to computational continuum mechanics using object-oriented techniques," Comput. Phys. **12**, 620 (1998).
[41]M.-J. Ni, R. Munipalli, P. Huang, N. B. Morley, and M. A. Abdou, "A current density conservative scheme for incompressible MHD flows at a low magnetic

Reynolds number. Part II: On an arbitrary collocated mesh," J. Comput. Phys. **227**, 205–228 (2007).
[42]N. Weber, P. Beckstein, V. Galindo, M. Starace, and T. Weier, "Electro-vortex flow simulation using coupled meshes," Comput. Fluids **168**, 101–109 (2018).
[43]R. Issa, A. Gosman, and A. Watkins, "The computation of compressible and incompressible recirculating flows by a non-iterative implicit scheme," J. Comput. Phys. **62**, 66–82 (1986).
[44]S. B. Pope and S. B. Pope, *Turbulent Flows* (Cambridge University Press, 2000).
[45]S. Gavrilakis, "Numerical simulation of low-Reynolds-number turbulent flow through a straight square duct," J. Fluid Mech. **244**, 101 (1992).
[46]J. L. Lumley, "Computational modeling of turbulent flows," Adv. Appl. Mech. **18**, 123–176 (1979).
[47]S. Kenjereš, "Energy spectra and turbulence generation in the wake of magnetic obstacles," Phys. Fluids **24**, 115111 (2012).